

Surface effects in layered semiconductors Bi_2Se_3 and Bi_2Te_3

S. Urazhdin, D. Bilc, S. D. Mahanti, and S. H. Tessmer

Department of Physics and Astronomy, Michigan State University, East Lansing, Michigan 48824, USA

Theodora Kyratsi and M. G. Kanatzidis

Department of Chemistry, Michigan State University, East Lansing, Michigan 48824, USA

(Received 3 December 2002; published 19 February 2004)

Scanning tunneling spectroscopy of Bi_2Se_3 and Bi_2Te_3 layered narrow gap semiconductors reveals finite in-gap density of states and suppressed conduction in the energy range of high valence-band states. Electronic structure calculations suggest that the surface effects are responsible for these properties. Conversely, the interlayer coupling has a strong effect on the bulk near-gap electronic structure. These properties may prove to be important for the thermoelectric performance of these and other related chalcogenides.

DOI: 10.1103/PhysRevB.69.085313

PACS number(s): 68.35.Dv, 68.37.Ef, 73.20.Hb, 71.55.Ht

I. INTRODUCTION

Narrow gap semiconductor Bi_2Te_3 alloys with Sb_2Te_3 and Bi_2Se_3 are classic room temperature thermoelectric materials.¹ Their excellent thermoelectric performance has been attributed to the details of the near-gap electronic structure combined with low lattice thermal conductivity. In spite of a long history of their research, there is an ongoing effort toward the detailed understanding of the near-gap electronic structure of Bi_2Te_3 and related materials,^{2–6} with the ultimate goal of improving the thermoelectric performance through the electronic structure engineering. Several features are of interest. According to de Haas–van Alphen experiments, both valence-band maximum (VBM) and conduction-band minimum (CBM) in Bi_2Te_3 are sixfold degenerate,⁷ which significantly improves thermoelectric performance.¹ It has proved to be difficult to reproduce this degeneracy with band-structure calculations. The relativistic corrections have been suggested³ to play an important role in the formation of the gap, in particular the degeneracy of band extrema. Calculations including spin-orbit interaction^{3–6} have successfully reproduced the sixfold degeneracy of the VBM. The details of the electronic structure, however, seem to be extremely sensitive to the calculation procedure, and only one published result reproduced the degeneracy of the CBM.⁶ The complicated nature of the near-gap electronic structure is also likely responsible for several yet unexplained experimentally observed effects, such as strong electron-phonon coupling, carrier concentration increase upon cooling³ in Bi_2Te_3 or upon application of external pressure in a related compound BaBiTe_3 .⁸

In this paper we present analysis motivated by the scanning tunneling spectroscopy (STS) study of Bi_2Te_3 and a similar compound Bi_2Se_3 . Although Bi_2Se_3 is not as technologically important as Bi_2Te_3 , both are very similar in terms of their structures and physics of the gap formation. The semiconducting gap in Bi_2Se_3 is larger than in Bi_2Te_3 , with nondegenerate band extrema. The spin-orbit correction in Bi_2Se_3 is not as important as in Bi_2Te_3 , making the band-structure calculations relatively more reliable.⁴ We therefore view Bi_2Se_3 as a model compound more easily accessible to both experimental and theoretical analysis.

To model the experimental STS data, we have performed first-principles electronic structure calculations in a slab geometry.⁹ Due to the strongly layered structure of Bi_2Te_3 and Bi_2Se_3 , the interlayer bonds are conventionally termed as Van der Waals type.^{3–6} Because of such weak interlayer bonding, the effect of the surface on the electronic structure is expected to be small. Such an assumption is made in most interpretations of the surface probes (e.g., electron tunneling and photoemission) of layered compounds.¹⁰ However, an increased attention has been recently given to the impact of the weak interlayer bonding on both bulk and surface electronic properties of layered materials.^{6,11} In a recent publication,¹² we have shown that surface electronic structure plays an important role in the observation of near-surface defects in Bi_2Se_3 . In this paper, we show that in Bi_2Te_3 and Bi_2Se_3 the surface effects dominate the near-gap electronic structure observed with STS. From this observation, we conclude that the interlayer coupling is important for the formation of the near-gap electronic structure in these layered compounds, both at the surface and in the bulk. This property of the strongly layered compounds may be the origin of several important physical effects.^{3,8}

II. EXPERIMENT

The crystal structure of both Bi_2Te_3 and Bi_2Se_3 is rhombohedral with space group $D_{3d}^5(R\bar{3}m)$.¹⁴ It can be represented as a stack of hexagonally arranged atomic planes, each consisting of only one type of atom. Five atomic planes are stacked in a close-packed fcc fashion in order [Fig. 1(a)] Te1(Se1)-Bi-Te2(Se2)-Bi-Te1(Se1), in a quintuple layer. The proximity of the surface breaks the equivalence of the Te1(Se1) positions in a layer, so throughout this paper we will use a Te3(Se3) notation for the third Te(Se) atomic plane from the surface. The hexagonal unit cell, shown in Fig. 1(a), spans three quintuple layers and contains 15 atoms.

Single crystal Bi_2Te_3 and Bi_2Se_3 samples used for scanning tunneling microscopy (STM) experiments were grown by a slow directional solidification technique. Bi_2Te_3 samples were naturally (through the formation of defects) p doped with carrier concentration of about 10^{19} cm^{-3} , while Bi_2Se_3 was naturally n doped with similar carrier concentra-

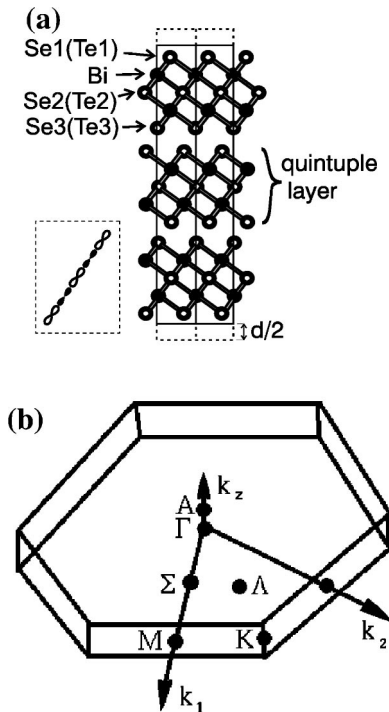


FIG. 1. (a) Bi_2Se_3 (Bi_2Te_3) structure viewed parallel to the layers. $2 \times 1 \times 1$ hexagonal unit cell is shown with a solid line. The unit cell used for slab calculations (for a three-layer slab) is shown in dash. In a dashed frame one of the $pp\sigma$ bonded chains is plotted. (b) Hexagonal Brillouin zone of Bi_2Se_3 (Bi_2Te_3).

tion. This difference is likely due to the high formation energy of Bi substitutional defects on Se sites (Bi_{Se} antisite defects) in Bi_2Se_3 ,¹⁵ which are acceptors. The crystals are strongly layered and can be easily cleaved with a scotch tape. The surface is sufficiently inert to obtain atomic resolution in air immediately after cleaving. However, to reduce the effects of adsorbates, the samples were cleaved in ultrapure He atmosphere in a glove box directly attached to the STM setup. The effective work function obtained by measuring the tunneling current vs the tip-sample separation was about 1 eV and showed no significant variation over the sample surface, indicating minimal surface contamination/oxidation. The STM measurements were performed using a custom built low-temperature microscope with direct immersion in liquid He-4.¹⁷ Chemically etched or cut PtIr STM tips were used with similar results.

An experimental STM topographic image of Bi_2Se_3 (0,0,1) surface is shown in Fig. 2(a). Figure 2(b) shows a simulated topographic image of Bi_2Se_3 surface. It was obtained from theoretical calculations in a slab geometry, as discussed in Sec. III, by integrating the energy projected charge density in a range of 0.7 eV from the top of the valence band, at a plane 2.4 Å above the surface Se atoms. In both the experimental and simulated topographic images, we identify the highest corrugations with the surface Se atoms. Both images Figs. 2(a) and 2(b) reflect the sixfold rotational symmetry of the surface Se plane. However, this sixfold symmetry is broken by the Bi atoms in the underlying atomic plane. Bi atoms are positioned in the center of every other

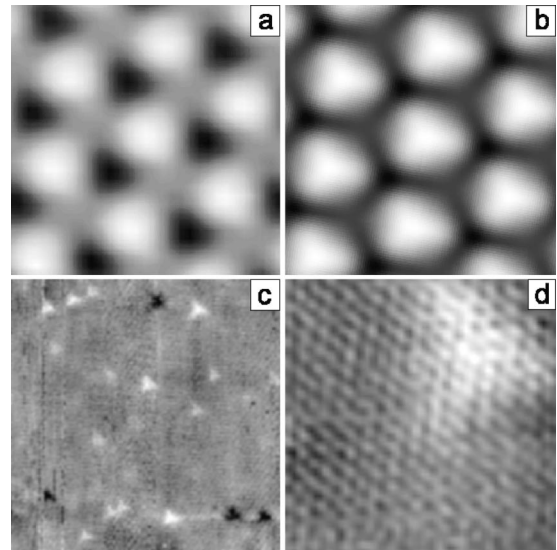


FIG. 2. (a) $1.3 \times 1.3 \text{ nm}^2$ topographic image of Bi_2Se_3 surface acquired at a bias voltage of -0.7 V . Black to white scale is 30 pm. Autocorrelation was used to enhance the image. (b) Calculated topography of Bi_2Se_3 at a bias voltage of -0.7 V . (c) $65 \times 65 \text{ nm}^2$ image of surface topographic defects in Bi_2Se_3 . (d) $6.5 \times 6.5 \text{ nm}^2$ image of one of the defect features.

triangle formed by the neighboring surface Se atoms, lowering the rotational symmetry to threefold. In the simulated image [Fig. 2(b)], the darkest spots between Se atoms correspond to positions which are not occupied by Bi in the second atomic plane, while positions occupied by Bi yield less contrast. We interpret our experimental image Fig. 2(a) similarly. The slight discrepancy between the shapes of the Se atomic corrugations is, in terms of the Fourier components of the topographic images, due to the higher harmonics, which are not manifested in the experiment.

Topographic images of Bi_2Se_3 show a small density of “triangular” defects, as illustrated in a large scale image, Fig. 2(c), and a smaller-scale image of one defect, Fig. 2(d). We observe both recessions [darker spots in Fig. 2(c)] and protrusions (brighter spots) in topography. Most of the defects appear as protrusions. These topographic defects can be contrasted to the clover-shaped impurity states, observed previously on Bi_2Se_3 doped with excess Bi,¹² and attributed to the substitutional Bi_{Se_3} impurities. Such substitutional defects did not result in measurable atomic displacements, and were observable with STM only at certain bias voltages, through the variation of the local electronic structure. In contrast, STS measurements, performed in the vicinity of defects shown in Figs. 2(c) and 2(d), reveal no significant variation of the local electronic structure. Thus, they are merely due to atomic displacements. We attribute them to interlayer Bi interstitial defects, located between the first and second (closest to the surface) quintuple layers. Such defects are energetically more favorable than the intralayer interstitials, due to the weak interlayer coupling.

The elastic strain, caused by such interstitial defects, is determined by the tensor of elastic susceptibility, which is related to the bonding scheme of the material.¹³ In Bi_2Se_3 , the $pp\sigma$ -bonded chains,¹² shown schematically in Fig. 1(a),

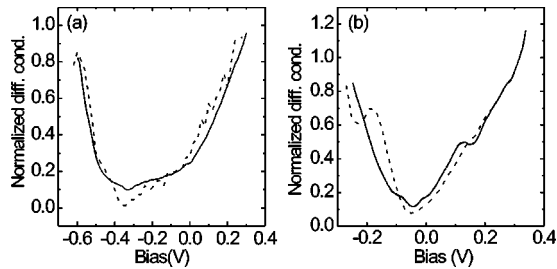


FIG. 3. (a) Solid lines: near-gap tunneling differential conductance dI/dV_B spectrum of Bi_2Se_3 , acquired directly with a lock-in detection technique at a temperature of 4.2 K. Dashed lines: theoretical curves, calculated as discussed in Sec. III. The curves are normalized by the differential conductance at $V_B=0.3\text{V}$. These plots are reproduced from Ref. 12. (b) Same as (a), for Bi_2Te_3 .

are the directions of the highest material stiffness. Strain due to the interlayer impurity atom propagates to the surface predominantly along the $pp\sigma$ chains in a characteristic triangular shape [Figs. 2(c) and 2(d)]. The orientation of the $pp\sigma$ chains, inferred from the defect images in Figs. 2(c) and 2(d), is consistent with the crystal orientation determined from the atomically resolved topographic images away from the defects [Fig. 2(a)].

The established bulk semiconducting gap value in Bi_2Se_3 is about 0.3 eV.^{4,15,16} The features in the typical tunneling differential conductance dI/dV_B spectra of atomically resolved Bi_2Se_3 surface [Fig. 3(a)] at sample bias voltages $V_B=0\text{V}$ and -0.35V likely correspond to the gap edges. However, conductance is finite at V_B between -0.35V , and 0.0V , indicating finite density of in-gap states. Another feature of the spectra shown in Fig. 3(a) is low conductance just below the gap, at V_B between about -0.5V and -0.35V . At the measurement temperature of 4.2 K, thermal broadening is negligible on the displayed bias voltage scale, so the spectra represent the local surface density of states. Typical differential conductance spectra of p -doped Bi_2Te_3 [Fig. 3(b)] exhibit features similar to spectra of Bi_2Se_3 : the conductance is finite at any V_B , and there is a pronounced feature at $V_B\approx 0.18\text{V}$, likely signifying the conduction-band bottom. The spectra presented in Fig. 3 are highly reproducible over the sample surface. This observation excludes the possibility that the finite in-gap conductance is due to impurity states, as was originally suggested to explain a similar finite density of in-gap states observed in photoemission experiments.¹⁸ The semiconducting gap of Bi_2Te_3 inferred from the differential conductance spectra agrees with the generally accepted value of about $0.15\pm 0.02\text{eV}$.³ As in Bi_2Se_3 , the conductance is suppressed at energies corresponding to tunneling from the high valence band (HVB) states. Model calculations discussed below suggest that these features are due to the surface effects, quite general to the layered chalcogenide compounds.

Due to the relatively weak interlayer bonding, our samples usually cleave between the quintuple layers. In Bi_2Te_3 samples doped with excess Te, we observe a small number of topographic steps with height smaller than the quintuple layer thickness. A topographic image Fig. 4(a) shows an area of n -type Bi_2Te_3 sample doped with 1.7%

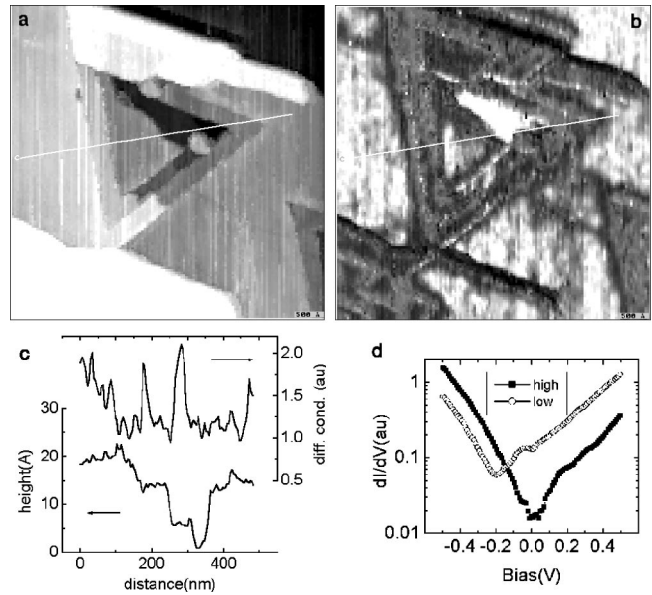


FIG. 4. (a) Topographic image of a $0.5\times 0.5\ \mu\text{m}^2$ area of a Bi_2Te_3 sample doped with 1.7% excess Te. The area has a high density of step edges and is not representative of the typical cleaved surface. Bias voltage $V=-80\text{mV}$. (b) A dI/dV_B map acquired simultaneously with (a). (c) Simultaneous cross sections through (a) and (b), as shown in (a) and (b) with a line. (d) Logarithmic plot of differential conductance spectra representative of high and low intensity areas in (b).

excess Te, exhibiting a particularly high density of such steps. The steps are arranged in a threefold symmetric fashion, with three apparent preferable step orientations. We correlate their orientations with the symmetry of the crystal, giving the easiest in-plane cleavage along hexagonal $[100]$, $[110]$, and $[010]$ directions.

Simultaneously with topographic measurement, we mapped local differential conductance of the surface as shown in Fig. 4(b). This measurement was performed by adding a small ac voltage of $V_B=-80\text{mV}$, and mapping the induced small ac tunneling current using standard lock-in detection. We use this technique to characterize the variation of the local electronic structure. On a surface cleaved between the quintuple layers, we do not expect to see any variation of the local differential conductance, even when topographic image shows steps corresponding to cleavage along different quintuple layers. The image Fig. 4(b), on the contrary, shows a clear contrast, correlated with the topographic variations in Fig. 4(a). The contrast results from the local surface electronic structure variation due to the different atomic termination of the surface. Thus, Fig. 4(b) is a direct experimental evidence of the termination-dependent surface states in Bi_2Te_3 .

Figure 4(c) shows a cross section both through topographic and conductance maps, as indicated in Figs. 4(a) and 4(b) with a line. The plot shows a direct correlation between the topographic steps and the measured value of the differential conductance. As also seen from the topographic curve in Fig. 4(c), the terrace step heights are smaller than the quintuple layer thickness of about $10\ \text{\AA}$, consistent with our interpretation of Fig. 4(b). To clarify the nature of the spec-

topographic variations, producing contrast in Fig. 4(b), in Fig. 4(d) we plot differential conductance spectra, acquired at points of the surface, corresponding to different intensities in Fig. 4(b). A typical differential conductance spectrum of a high intensity area [solid symbols in Fig. 4(d)] smoothly rises at negative V_B , and exhibits a minimum at $V_B=0$ and a weak feature at $V_B \approx 0.18$ V. This spectrum is typical of most of the sample surface, and is very similar to the spectra of p -doped Bi_2Te_3 , shown in Fig. 3. Differential conductance spectra, characteristic of the low intensity areas in Fig. 4(b) [open symbols in Fig. 4(d)], rise smoothly at positive V_B , and exhibit a feature at $V_B=0$ and a minimum at $V_B = -0.18$ V. These spectra are characteristic of a small percentage of the sample surface, which we identify with areas terminated with intralayer atomic planes. Identifying the lower and the higher bias features in the spectrum with the valence band maximum and conduction band minimum, correspondingly, we can interpret the spectra shown in Fig. 4(d) in terms of the surface-induced band bending. The Fermi level is pinned at the surface by the surface states either to the CBM [open symbols in Fig. 4(d)], or VBM [solid symbols in Fig. 4(d)]. In particular, the p -like spectra of most of the n -doped sample surface are evidence for the conduction-like surface states, present at the surface cleaved between the quintuple layers. Such empty states lead to the surface pinning of the Fermi level to the VBM. This conclusion is consistent with our calculations of the surface states, described below. The difference between the spectra in Fig. 4(d) can be understood as an almost rigid shift by the value of the semiconducting gap (≈ 0.18 eV). The more subtle termination-dependent variations of the surface electronic structure result in other differences between these spectra.

III. THEORY

We modeled our STS results with electronic structure calculations based on density functional theory.¹⁹ Self-consistent full-potential linearized augmented plane wave formalism (LAPW) (Ref. 20) was used, with the generalized gradient approximation (GGA) for the exchange and correlation potential.²¹ Convergence of the self-consistent iterations was verified to within 1 meV for 21 k points inside the reduced Brillouin zone, with a cutoff of -81.6 eV between the valence and the core states. Scalar relativistic corrections were included and spin-orbit interaction was incorporated using a second variational procedure.²² The calculations were performed with commercially available software.²³ For the band-structure calculations of the bulk Bi_2Se_3 and Bi_2Te_3 we used a hexagonal unit cell consisting of three quintuple layers [see Fig.1(a)]. Experimental values of the lattice constants were used. To model the surface, we used a repeating slab geometry⁹ with slabs consisting of 3, 6, and 12 quintuple layers separated by an increased distance d [Fig.1(a)], as compared to the bulk crystal structure. The calculated band structures did not exhibit significant variation with the separation larger than 0.4–0.5 nm between the slabs; therefore we found the slab separation of 0.7 nm, used for the calculations presented below, sufficient for modeling the surface. Relaxation calculations were performed for the three-

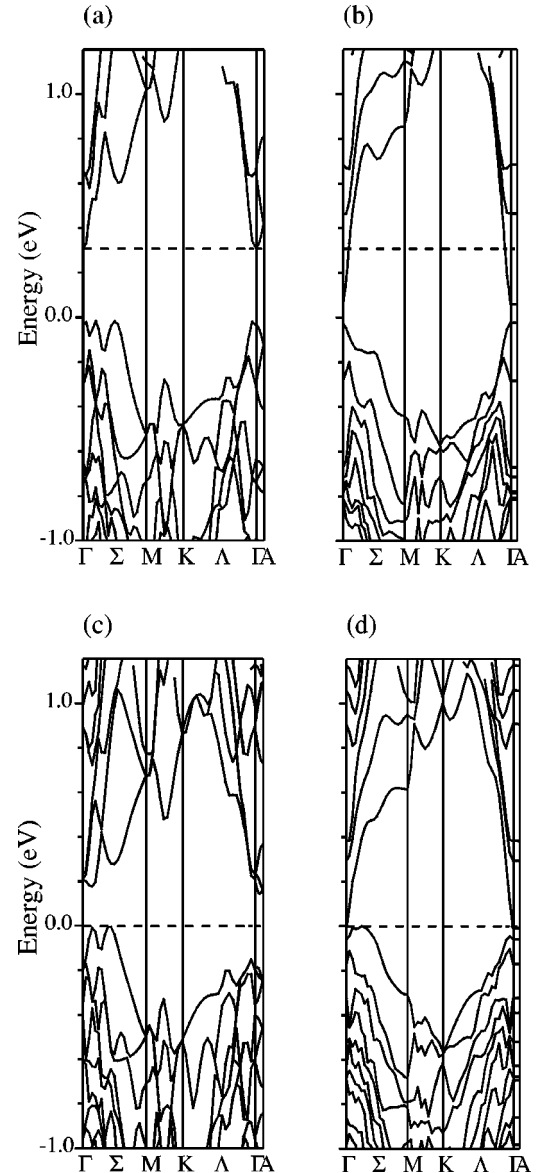


FIG. 5. Calculated band structure: (a) bulk Bi_2Se_3 , (b) three-layer slab of Bi_2Se_3 , (c) bulk Bi_2Te_3 , (d) three-layer slab of Bi_2Te_3 . The experimental Fermi energies are shown in dashed lines; zero energy corresponds to the top of the valence band.

slab geometry to see their effects on the surface electronic structure. These results are given at the end of this section.

In Fig. 5 we present the calculated band structures of Bi_2Se_3 and Bi_2Te_3 both in the bulk and slab geometries. Since the bulk unit cell spans three quintuple layers, the three-layer slab geometry used in Fig. 5 gives the same number of bands as in the bulk calculations, which is convenient for a direct comparison. It can also be speculated that due to the weak interlayer bonding the electronic states of the middle layer in a slab are close to the bulk states, and thus a three-layer slab might be sufficient for modeling the surface electronic structure of a bulk sample. We show below, that this can be accepted with certain limitations. Our calculations of the bulk band structure, shown in Figs. 5(a) and 5(c), yield a direct band gap of 0.3 eV in Bi_2Se_3 and an indirect

gap of 0.14 eV in Bi_2Te_3 with degenerate VBM, in reasonable agreement with the experimental values.^{3,16} They are close to the earlier theoretical results.³⁻⁵ Our calculation does not reproduce the sixfold degeneracy of the CBM in Bi_2Te_3 . This problem has been encountered in a number of earlier calculations.^{3-5,24} However, this discrepancy is not important for the general surface effects discussed in this paper. Comparing the calculations of the bulk band structure [Figs. 5(a) and 5(c)] with the slab [Figs. 5(b) and 5(d)], one finds that there is a significant effect of the reduced interlayer bonding between the slabs both in Bi_2Se_3 and Bi_2Te_3 . Orbital character analysis of the band structure and density of states (DOS) shows that the most notable differences are lowering of the bulk conduction band states into the gap and a drastic restructuring of the valence band, with most of the HVB states associated with surface Se1(Te1) atoms lowered in energy as compared to the bulk band structure. The remaining HVB states are dominated by the Se(Te) orbitals of the atoms located in the quintuple layers away from the surface, and as a consequence have a small amplitude at the surface. These observations are in agreement with experimental results presented in Sec. II: a finite density of states in the gap and a suppressed conduction in the HVB energy range.

The nature of the surface states can be elucidated through the analysis of their orbital character in real space and dispersion in the reciprocal space. As follows from Figs. 5(b) and 5(d), the in-gap states are highly dispersive in the plane parallel to the quintuple layers [ΓM and ΓK directions in the Brillouin zone, Fig. 1(b)], indicating that they originate from the strong in-plane hybridization of the surface atoms.

Analysis of the orbital character of the in-gap states shows that they are dominated by the two closest to the surface atomic positions: Se1 and Bi in Bi_2Se_3 , and Te1 and Bi in Bi_2Te_3 . However, there are significant contributions from all the atoms in the surface layer. The in-gap states do not exhibit dispersion in the direction perpendicular to the quintuple layers (the ΓA direction), which is consistent with the negligible interaction between the slabs. The lowering of the HVB at the surface is a robust effect which has been qualitatively understood in terms of a simple one-dimensional tight-bonding model.¹² The analysis of the orbital character of the HVB for the bulk Bi_2Se_3 (Bi_2Te_3) shows that they are dominated by Se(Te) states, which are antibonding in the sense of the interlayer coupling. Consequently, at the surface, the energy of such states is reduced.

To follow the evolution of the electronic structure with the distance from the surface, in Fig. 6 we plot the partial “atomic” DOS of Se1 atoms for various quintuple layers as a function of their position relative to the surface in a 12 slab-geometry calculation. The in-gap states associated with the lowering of the bulk conduction band into the gap (the states between 0 eV and 0.25 eV) are mostly present in the first quintuple layer. There are also in-gap states associated with the restructuring of the HVB (the states between -0.07 eV and 0 eV, insert in Fig. 6). The bulk HVB states (below -0.07 eV) are almost recovered by the Se1 at the second layer from the surface, while the surface Se1 contribution to the states near the top of the valence band (between

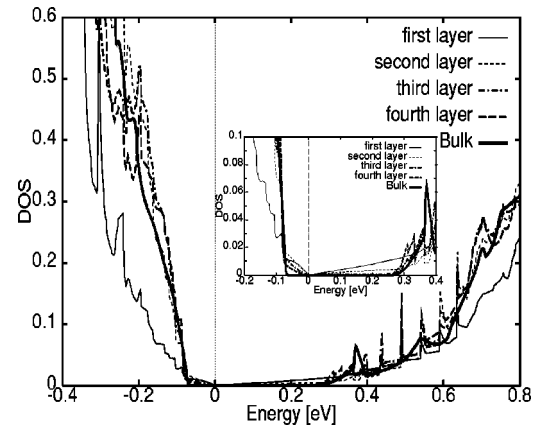


FIG. 6. Partial DOS of Se1 in Bi_2Se_3 for various positions of the quintuple layers with respect to the surface in a 12-slab geometry.

-0.07 eV and -0.3 eV) is dramatically suppressed. This is consistent with the antibonding, in the sense of interlayer bonding, nature of the states near the top of the valence band, as found, e.g., in tight-bonding calculations.¹²

The sharp peaks, which are present in the DOS calculations in slab geometry, occur due to the saddle points, where the bands have no dispersion along the ΓA direction. According to Gofron and Dabrowsky,²⁵ such saddle points, which they called “extended” Van Hove singularities, yield a power-law divergence in DOS. These are artifacts due to the approximation of the bulk sample terminated with a surface by a finite thickness slab. The number of peaks increases with the slab thickness due to the folding of the Brillouin zone along the ΓA direction, while their weight decreases. In the limit of an infinite slab, the DOS should become smooth. The deviation from the bulk DOS in the case of Se1 atoms located at second, third and fourth layer are particularly strong in the HVB between -0.3 eV and -0.1 eV and are due to these extended Van Hove singularities.

The conductance spectrum gives information about local DOS and for a qualitative comparison we have used a three-slab geometry to compute the conductance spectra. To simulate the experimental differential conductance spectra, we have calculated the electronic charge as a function of energy, $\rho(\vec{r}, E)$, at a point located at 2.35 \AA above the surface Se atom. This was done by calculating $\rho(\vec{r}, E)$ for different values of E within a energy mesh of 20 meV and then averaging over five energy intervals. The theoretical conductance spectra was obtained by multiplying $\rho(\vec{r}, E)$ by a scale factor to give an overall fit to the experiment. To simulate the conductance spectra a very dense mesh of 961 irreducible k points in the $k_z=0$ plane of the Brillouin zone was required and in order to reduce the computational time we used the three-slab geometry to model the surface. The calculated and experimental conductance spectra of Bi_2Se_3 and Bi_2Te_3 are given in Fig. 3. The theoretical values were shifted in order to match the Fermi energies. The calculated conductance spectra clearly show finite in-gap density of states in both Bi_2Se_3 and Bi_2Te_3 . The overall agreement in Bi_2Se_3 is quite remarkable, while for Bi_2Te_3 the agreement is not as good.

We have also modeled the dependence of the electronic

structure on the surface termination (Fig. 4), by calculating the band structure of Bi_2Te_3 in slab geometry with slabs terminated with Bi2. The calculation supports the qualitative picture based on simple electron counting arguments that the Bi-terminated surface creates excess electrons, resulting in a shift of the Fermi level into the conduction band. This is consistent with the local shift of the conductance spectra [Fig. 4(d)].

To see the effects of structural relaxation on the electronic states, we performed volume optimization (i.e., optimization with respect to scaling of the lattice constants), and force minimization for individual atomic sites up to 0.2 mRy/nm for the three-slab geometry. Optimization decreases the volume by 1% for Bi_2Se_3 and increases by 4% for Bi_2Te_3 . All the optimized bond distances, except for the interlayer bonds, are within 1–2.5% of their bulk values both in Bi_2Se_3 and Bi_2Te_3 . The interlayer distances within the slabs increase by 7.9% and 5.5% in Bi_2Se_3 and Bi_2Te_3 , correspondingly. The relaxation does not significantly change the effects of the surface on the electronic band structure. In Bi_2Se_3 , the lowering of the surface conduction band into the bulk gap is reduced from ~ 0.25 eV in unrelaxed calculation to ~ 0.17 eV after relaxation is performed, while the other changes in the band structure are insignificant. In Bi_2Te_3 , the only significant effect of the relaxation is a slight upward shift of the highest valence band by ~ 0.03 eV. The small effect of structural relaxation reflects the weakness of interlayer bonds, i.e., the relatively small structural perturbation introduced by the presence of the surface.

IV. SUMMARY AND DISCUSSION

We have interpreted STS observations of finite in-gap conduction and suppressed conduction near the top of the valence band in Bi_2Te_3 and Bi_2Se_3 in terms of the surface electronic structure. Surface states appear in the theoretical calculations which are in agreement with STS observations. The calculations show that the surface states extend into the

first quintuple layer with a decay length of about 1 nm. These surface effects are complimentary to the strong influence of the inter(quintuple) layer bonding on the *bulk* electronic structure of these compounds, rendering the intuitive picture of layers weakly bonded with Van der Waals type interaction inadequate. There is an important covalent contribution to the inter(quintuple) layer bonding. This can also be seen from the Fermi surface characteristics.⁶

Finally, we would like to make some general remarks regarding the properties of these layered compounds related to the effect of the interlayer coupling on the electronic structure. The small value of the elastic constant associated with the weak interlayer coupling results in strong variation of the valence band electronic structure with external conditions: temperature,³ external pressure,⁸ or chemical pressure in alloys. The anomalous electron coupling to the heavy phonon branch associated with interlayer distance variation likely results in strong electron-phonon scattering.³ An important consequence for the thermoelectric properties is the possibility of a large phonon drag contribution to the thermopower.²⁶ In Bi_2Te_3 , the effect should be particularly strong due to the small value of the semiconducting gap and large interlayer spacing (and correspondingly weak interlayer coupling). Lastly, this study suggests that applications of low-dimensional narrow gap semiconductor structures²⁷ for thermoelectric devices where interface effects play an important role, cannot rely on the assumption that bulklike electronic properties persist in low-dimensional structures.

ACKNOWLEDGMENTS

We acknowledge helpful discussions with Norman O. Birge, M. I. Dykman, T. Hogan, and S. Lal. This work was supported in part by NSF Grants Nos. DMR-0075230 and DMR-0305461, and Michigan State University. Financial support from the Office of Naval Research (Contract No. N00014-02-1-0867) is gratefully acknowledged. S.H.T. acknowledges support of the Alfred P. Sloan Foundation.

¹G.D. Mahan, *Solid State Physics* (Academic Press, Orlando, 1998), Vol. 51; M.G. Kanatzidis, *Semicond. Semimetals* **69**, 51 (2001).

²P. Pecheur and G. Toussaint, *Phys. Lett. A* **135**, 223 (1989).

³G.A. Thomas, D.H. Rapke, R.B. Van Dover, L.F. Mattheis, W.A. Surden, L.F. Schneemaper, and J.V. Waszczak, *Phys. Rev. B* **46**, 1553 (1992).

⁴S.K. Mishra, S. Satpathy, and O. Jepsen, *J. Phys.: Condens. Matter* **9**, 461 (1997).

⁵P. Larson, S.D. Mahanti, and M.G. Kanatzidis, *Phys. Rev. B* **61**, 8162 (2000).

⁶S.J. Youn and A.J. Freeman, *Phys. Rev. B* **63**, 085112 (2001).

⁷H. Kohler, *Phys. Status Solidi B* **73**, 95 (1976); B. Shoeder, A. Von Middendorff, H. Kohler, and G. Landwehr, *ibid.* **59**, 561 (1973); H. Kohler, *ibid.* **74**, 591 (1976).

⁸J.F. Meng, N.V. Chandra Shekar, J.V. Badding, D.-Y. Chung, and M.G. Kanatzidis, *J. Appl. Phys.* **90**, 2836 (2001).

⁹J. Tersoff and D.R. Hamann, *Phys. Rev. Lett.* **50**, 1998 (1983).

¹⁰For example, all interpretations of photoemission and STM data on high-temperature superconductors that we are aware of.

¹¹A. Klein, S. Tiefenbacher, V. Eyert, C. Pettenkofer, and W. Jaegerman, *Phys. Rev. B* **64**, 205416 (2001).

¹²S. Urazhdin, D. Bilc, S.H. Tessmer, S.D. Mahanti, T. Kyratsi, and M.G. Kanatzidis, *Phys. Rev. B* **66**, 161306(R) (2002).

¹³W.A. Harrison, *Electronic Structure and the Properties of Solids* (Freeman, San Francisco, 1980).

¹⁴R.G. Wyckoff, *Crystal Structures* (Wiley, New York, 1967), Vol. 2.

¹⁵D.R. Lovett, *Semimetals and Narrow-Bandgap Semiconductors* (Pion Limited, London, UK, 1977).

¹⁶J. Black, E.M. Conwell, L. Seigle, and C.W. Spencer, *J. Phys. Chem. Solids* **2**, 240 (1957).

¹⁷S.H. Tessmer, D.J. Van Harlingen, and J.W. Lyding, *Rev. Sci. Instrum.* **65**, 2855 (1994).

- ¹⁸V.A. Greanya, W.C. Tonjes, Rong Liu, C.G. Olson, D.-Y. Chang, and M.G. Kanatzidis, *Phys. Rev. B* **62**, 16 425 (2000).
- ¹⁹P. Hohenberg and W. Kohn, *Phys. Rev.* **136**, B864 (1964); W. Kohn and L. Sham, *Phys. Rev.* **140**, A1133 (1965).
- ²⁰David J. Singh, *Plane Waves, Pseudopotentials and the LAPW Method* (Kluwer Academic Publishers, Boston, 1994).
- ²¹J.P. Perdew, K. Burke, and M. Ernzerhof, *Phys. Rev. Lett.* **77**, 3865 (1996).
- ²²D.D. Koelling and B. Harmon, *J. Phys. C* **13**, 6147 (1980).
- ²³P. Blaha, K. Schwarz, and J. Luitz, *WIEN97, A Full Potential Linearized Augmented Plane Wave Package for Calculating Crystal Properties* (Karlheinz Schwarz, Techn. Universitat Wien, Austria, 1999), ISBN 3-9501031-0-4.
- ²⁴Our calculations reproduce the sixfold degeneracy of the CBM when the $p_{1/2}$ relativistic local orbitals are incorporated in the LAPW basis. The band gap is reduced from 0.14 eV to 60 meV.
- The sixfold degenerate conduction band and a similar small gap of 61 meV were found by Youn *et al.* (Ref. 6). The smaller value of the gap vis-a-vis experiment is consistent with our understanding of the underestimation of the band-gap value in GGA. S.D. Mahanti, P. Larson, D. Bilc, and H. Li, *Proceedings of the Chemistry, Physics and Materials Science of Thermoelectric Materials: Beyond Bismuth Telluride* Traverse City, 2002 (Kluwer Academic, New York, 2003).
- ²⁵K. Gofron, J.C. Campuzano, A.A. Abrikosov, M. Lindroos, A. Bansil, H. Ding, D. Koelling, and B. Dabrowski, *Phys. Rev. Lett.* **73**, 3302 (1994).
- ²⁶Frank J. Blatt, *Physics of Electronic Conduction in Solids* (McGraw-Hill, New York, 1968).
- ²⁷L.D. Hicks and M.S. Dresselhaus, *Phys. Rev. B* **47**, 12 727 (1993); L.D. Hicks and M.S. Dresselhaus, *ibid.* **47**, 16 631 (1993).